Laser-induced controllable crystallization of organic-inorganic hybrid perovskites assisted by gold nanoislands

Junying Chen,[1] Jiaxin Yang,[1] Weijie Zhuang,[1] Xiaobing He,[1] Shulei Li,[2] Zhenxu Lin,[1,3] and Sheng Lan[1,*]

[1]*Guangdong Provincial Key Laboratory of Nanophotonic Functional Materials and Devices, School of Information and Optoelectronic Science and Engineering, South China Normal University, Guangzhou 510006, P. R., China*

[2]*School of Optoelectronic Engineering, Guangdong Polytechnic Normal University, Guangzhou 510665, P. R., China*

[3]*linzhenxu2013@163.com*

[*]*slan@scnu.edu.cn*

Abstract: Organic-inorganic hybrid perovskites have attracted great interest in recent years because of their excellent luminescence properties. However, the controllable and reversible growth of such perovskites by using a simple method remains a big challenge although it is highly desirable. Here, we demonstrate the controllable and reversible crystallization of MAPbBr$_3$ in a thin liquid film on top of densely-packed gold (Au) nanoislands deposited on a silica substrate. The formation of MAPbBr$_3$ crystal is induced by irradiating densely-packed Au nanoislands with femtosecond laser light. MAPbBr$_3$ crystals with diameters of ~10 μm can be stably created around the focal point of the laser beam and they will disappear rapidly after switching off the laser light. The threshold laser power for creating stable MAPbBr$_3$ crystal depends strongly on the morphology of Au nanoislands, which can be modified by changing the sputtering time. By increasing the concentration of the precursors in the liquid film, high-quality MAPbBr$_3$ microrods can be obtained after switching off the laser light. Our findings indicate a simple but effective method to induce perovskites with a controllable manner and pave the way for developing photonic devices based on organic-inorganic perovskites.

1. Introduction

Due to their excellent physical properties, perovskites have attracted much attention in recent years and great progress has been made in the research and development of solar cells [1–3], light-emitting diodes [4–6], lasers [7–10], optical sensors [11–13], and coolers [14–16]. Since perovskites generally possess low thermal conductivity (lower than silica) and high defect tolerance, it was found that perovskite metasurfaces preserving highly efficient luminescence can be fabricated by femtosecond laser lithography [13]. In addition, the temperature distribution induced by femtosecond laser light was exploited as the driving force for ion migration in transparent dielectric media [14]. By utilizing the inherent ionic nature and the low formation energy of perovskite, highly luminescent CsPb(Cl/Br)$_3$ quantum dots was reversibly fabricated in situ and decomposed through femtosecond irradiation and thermal annealing [15,16]. In these cases, the preparation and morphology of perovskite can be effectively controlled by the photothermal effect of laser irradiation.

In recent years, organic-inorganic hybrid perovskites CH$_3$NH$_3$PbX$_3$ (X = Cl, Br, I) have become the focus of many studies due to their potential applications in a variety of functional devices [14–16]. The great interest in such organic lead trihalide perovskites arises from their tunable optical properties, high absorption coefficients, long-range balanced electron and hole

transport [17], and simple preparation techniques with low cost [18–20]. In particular, it has been shown that MAPbBr$_3$ and MAPbI$_3$ single crystals have long carrier diffusion lengths and low trap-state densities, which are comparable to the state-of-the-art silicon photovoltaics [21]. These unique properties make MAPbX$_3$ single crystals highly desirable semiconductors for photovoltaic applications much broader than their polycrystalline thin film counterparts. Recently, single-crystalline thin films of hybrid organic-inorganic perovskite were successfully fabricated and they were used to demonstrate high-performance photodetectors [22]. In addition, a high-performance flexible photodetector with prevailing bending reliability and significantly increased responsivity was realized by using an ultrathin single-crystalline perovskite film (∼20 nm) as the active layer [23]. Moreover, it was demonstrated that a metasurface made of hybrid organic−inorganic perovskite can significantly enhance broadband absorption and improve photon-to-electron conversion, leading to a photodetector with enhanced photocurrent [24].

So far, various methods have been developed for the growth of organic-inorganic hybrid perovskites, including chemical vapor deposition, cooled crystallization, antisolvent vapor-assisted crystallization, and inverse-temperature crystallization (ITC). For example, MAPbBr$_3$ nanosheets were grown on a mica substrate by controlling the evaporation rate of the solvent (hydrobromic acid (HBr, 48wt.%) and N,N-Dimethylformamide (DMF, 57wt.%)) with the temperature [25]. More importantly, quasi-static solution growth of MAPbBr$_3$ sheets was achieved by placing a thin film of the solution on a hot plate and heated to 30 °C for more than 10 h. The thickness and the area of MAPbBr$_3$ sheets could be tuned by adjusting the volume of the solvent, heating temperature, and growth time [23]". Among these methods, ITC is one of the most commonly used methods, which exploits the reduced solubility of a perovskite in a solvent with increasing temperature to achieve the crystallization of the perovskite. It can be used to rapidly produce MAPbBr$_3$ and MAPbI$_3$ single crystals in hot solutions [26]. Although the growth of perovskite crystals by using the ITC method is very fast, the as-prepared perovskites exhibit carrier transport properties comparable to those prepared by using other techniques. The crystal growth rate of ITC exceeds the value reported previously for the method of using mixed perovskite single crystals, representing a major breakthrough in the synthesis of perovskite single crystals. However, the quality of perovskite single crystals grown by the ITC method needs to be further improved. In addition, it remains a challenge to accurately control the position and size of the perovskite single crystals.

It is well known that temperature is an important physical parameter needed to be controlled in crystal growth. The crystallization of perovskite by using the ITC method is usually realized by heating the solvent with an electric heater. In practice, a simple and convenient way for achieving the local heating of a material is laser irradiation. In particular, a localized temperature field can be established by irradiating a metallic nanoparticle with laser light. Owing to the existence of surface plasmon resonances in the metallic nanoparticle, it can effectively absorb the laser light and generate heat via the nonradiative recombination of carriers. For this reason, metallic nanoparticles have been successfully applied in photothermal therapy of cancer cells. The nanoscale temperature gradient generated by laser irradiation not only modifies the morphologies of metallic nanoparticles [27,28] but also facilitates the growth of functional nanomaterials, such as metal-oxide core-shell structures [29,30]. The reshaping of metallic nanoparticles by laser irradiation is also exploited to realize nanoscale optical display and storage [31]. A spatially localized temperature field can be used to produce luminescent carbon quantum dots by exploiting the Fano resonances formed in the clusters of metallic nanoparticles [32]. Moreover, the plasmon photothermal effect has been confirmed as an activation mechanism for photochemical reactions by exploiting the excitation of surface plasmon resonances [33–35]. In recent years, this plasmonic heating effect at the nanoscale has been successfully employed to realize nanophase engineering in a TiO$_2$ film and nanopoling in a poly(vinyl difluoride) film [36,37], which exhibits potential applications in photocatalysis, hot-electron chemistry, piezoelectronic devices, high-density data

storage, and anti-counterfeiting. In addition, nanoscale plasmonic dynamite was demonstrated by using $Au@C_{60}$ core-shell nanoparticles irradiated by laser light, which can be exploited as a powerful energy source for nanoactuation and nanomigration [38].

Recently, densely-packed gold (Au) nanoislands deposited on a silica (SiO_2) substrate have been confirmed as an ideal platform to realize high-quality optical storage and laser writing of perovskites [39,40]. Absorption of laser light can be greatly enhanced by the plasmonic hot spots induced by the coupling of Au nanoislands [41], facilitating the establishment of spatially localized temperature field by using laser irradiation. The temperature rise can be adjusted by controlling the morphology of densely-packed Au nanoislands.

Very recently, controllable and reversible crystallization of an all-inorganic perovskite ($CsPbBr_3$) has been successfully demonstrated by exploiting the plasmonic hot spot created at the contact point between a polycrystalline $CsPbBr_3$ nanosphere and a thin Ag film. Formation of $CsPbBr_3$ single crystal from $CsPbBr_3$ quantum dots was induced by laser irradiation and its size could be controlled by the laser power, leading to a dual-wavelength emission from the $CsPbBr_3$ nanosphere. However, perovskite nanocrystals prepared by utilizing the photothermal effect of metallic nanostructures has not yet be achieved [42]. At present, the reversible crystallization of perovskites induced by laser irradiation requires complex sample preparation process [43] or strict vacuum environment [44].

In this work, we employ densely-packed Au nanoislands as a plasmon-driven nanoreactor to realize the controllable formation of an organic-inorganic hybrid perovskite ($MAPbBr_3$). Such Au nanoislands can effectively absorb the photon energy of femtosecond laser light in the near infrared spectral range, creating a localized temperature field on the surface of Au nanoislands. We manipulate the local temperature field on the surface of Au nanoisland by adjusting the intensity of laser irradiation and realize the controllable and reversible crystallization of $MAPbBr_3$ in N, N-dimethylformamide (DMF) transparent solution [26,45]. $MAPbBr_3$ crystals with finite sizes can be stably created around the focal point of the laser beam once the laser power exceeds a critical value. They will be dissolved back into the solution if the laser light is switched off. In addition, high-quality $MAPbBr_3$ microrods can be obtained by laser irradiation by increasing the concentration of the precursors. These results provide a new way for studying the thermal stability of perovskites and promote the development of controlled growth of perovskites driven by surface plasmon.

2. Materials and methods

2.1. Sample preparation

The densely-packed Au nanoislands used to induce the crystallization of $MAPbBr_3$ crystal were deposited on SiO_2 substrates by using sputtering. The morphology of Au nanoislands was controlled by changing the sputtering time. The precursors used to synthesize $MAPbBr_3$ crystal (MABr and $PbBr_2$) were dissolved in a DMF solution with a specific concentration. In experiments, the DMF solution was dropped on Au nanoislands and covered with a glass slide, forming a thin liquid film. In this work, we did not observe the etching of Au nanoislands by the liquid film containing MABr and $PbBr_2$. The transmission spectrum of the Au film loaded with the liquid film remains unchanged for a long time.

2.2. Optical characterization

Femtosecond laser pulses with a wavelength of 800 nm, a repetition rate of 76 MHz, and a duration of 130 fs (Mira 900S, Coherent) was used to induce the crystallization of $MAPbBr_3$ crystal in the thin DMP layer formed on Au nanoislands. The femtosecond laser light was introduced into an inverted microscope (Observer A1, Zeiss) and focused on the sample surface by using a 100× objective lens. The generated optical signals were collected using the same

objective lens and directed to a spectrometer (SR-500i-B1, Andor) for spectrum analysis. The transmission spectra of the laser-induced $MAPbBr_3$ crystals were also measured by using the same microscope. The two-photon-induced luminescence (TPL) of $MAPbBr_3$ crystal was also excited by using the femtosecond laser light and analyzed by using the spectrometer.

2.3. Numerical simulation

The reflection, transmission, and absorption spectra of densely-packed Au nanoislands were numerically calculated by using the finite-difference time-domain (FDTD) technique (FDTD solution, https://www.lumerical.com). Based on the finite element method (FEM), the electric field and temperature distributions of Au nanoislands were numerically simulated by using commercially developed software (COMSOL Multiphysics v5.6, https://www.comsol.com.). The minimum mesh size was chosen to be 1.0 nm. A perfectly matched layer boundary condition was used to ensure the absorption of all outgoing radiation. Due to the small size of the nanoparticles and the good electrical conductivity of Au, it was assumed that the temperature inside each Au nanoparticle is uniform.

3.   Results and discussion

As mentioned at the beginning, the rapid growth of $MAPbBr_3$ single crystal can be realized by using the ITC method by properly selecting solvent and deliberately controlling temperature. In previous studies, high-quality perovskites were obtained by heating the solution of precursors in an oil bath [26,45,46]. In this case, the location of the perovskite crystal formed in solution is random and its size is difficult to control. Among many factors that affect the position and growth rate of the perovskite crystal, temperature is no doubt the most important one. For this reason, we employ laser irradiation of metallic nanoparticles as the method for controlling the temperature in the solution. The major advantage of this method is the introduction of spatially localized temperature field in the solution in a simple, efficient, fast, dynamical, and reversible way. This feature offers us the opportunity for selecting the position for inducing crystallization and controlling the size of the formed perovskite crystal. In addition, it enables the formation of high-quality perovskite crystals from a solution.

In Fig. 1, we present a schematic illustrating the growth of a $MAPbBr_3$ crystal in a thin layer of DMF solution containing MABr and $PbBr_2$ induced by laser irradiation. The substrate used to support the thin layer of DMF solution is obtained by depositing densely-packed Au nanoislands on a SiO_2 slide by sputtering. The morphologies of Au nanoislands can be controlled by adjusting the sputtering time. The spatially localized temperature field, which is used for realizing the crystallization of $MAPbBr_3$, is generated by irradiating Au nanoislands with 800-nm femtosecond laser pulses. Meanwhile, TPL is generated from the as-prepared $MAPbBr_3$ crystal under the excitation of femtosecond laser pulses. The $MAPbBr_3$ crystal will be dissolved back into the solution once the laser light is switched off. During this process, Au nanoislands are thermally shaped by laser irradiation and transformed into isolated Au nanoparticles. Finally, Au nanoparticles encapsulated by reduced precipitated reactants are left due to the reducibility of the DMF solution [47].

We first compared the absorption spectra simulated and measured for densely-packed Au nanoislands obtained by using different sputtering times ($T = 20$, 30, and 40 s), as shown in Fig. 2(a). The transmission electron microscopy (TEM) images of the Au nanoislands were used to build the physical models for the numerical simulations. Previously, closely-packed Au nanoislands prepared by the same method have been employed to realize high-density optical data storage [31]. The morphology of Au nanoislands was analyzed based on the TEM images. It was found that the size and filling ratio of Au nanoislands increase with increasing sputtering time. In the physical model used to simulate the absorption spectra of different samples, the height of all Au nanoislands is assumed to be the same (10 nm) because only the top view of Au
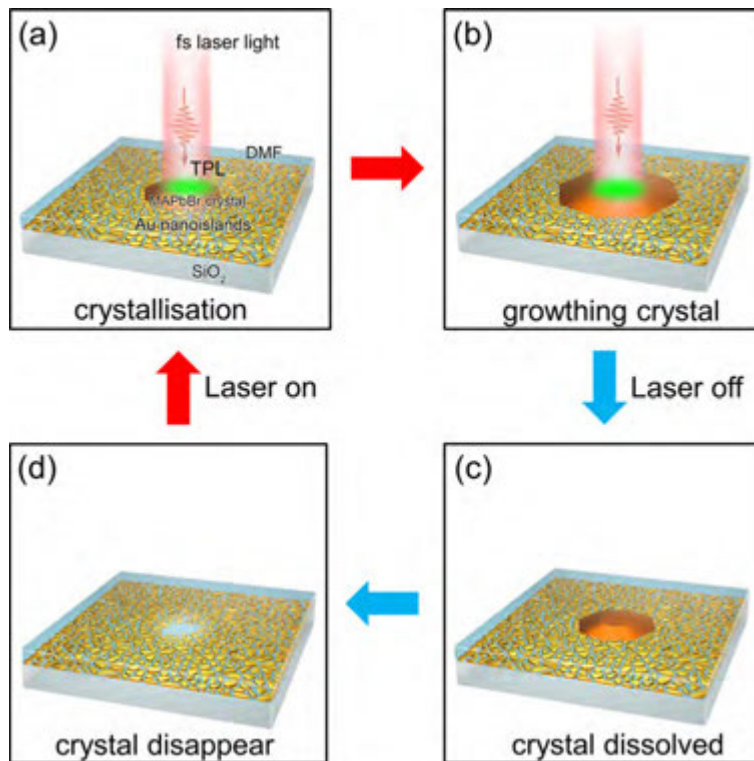
Fig. 1. Schematic illustrating the controllable and reversible crystallization of MAPbBr$_3$ induced in a transparent solution by irradiating densely-packed Au nanoislands with femtosecond laser light.

nanoislands can be obtained from the TEM images. Since the morphology of Au nanoislands plays an important role in determining the hot spots induced by the plasmonic coupling between Au islands, the discrepancy between the simulated and measured results is caused mainly by the inaccuracy in the morphology of Au nanoislands, especially their heights. It is noteworthy that the Au nanoislands with $T = 30$ s possess the largest absorption at ~800 nm, implying the most efficient absorption of the 800-nm femtosecond laser pulses. To further confirm this, we also simulated the temperature distributions in the Au nanoislands induced by the irradiation of a 800-nm laser beam with a Gaussian intensity distribution, as shown in Fig. 2(b-d). The diameter of the laser beam is assumed to be 1.0 µm. In all cases, a localized temperature distribution is observed. As expected, the highest temperature is achieved in the Au nanoislands with $T = 30$ s. With increasing sputtering time, the average size of Au nanoislands is increased. As a result, the plasmonic coupling between neighboring Au nanoislands is enhanced, leading to the increase in the number of plasmonic hot spots and thus the optical absorption. However, a further increase in the sputtering time leads to the merge of small nanoislands into large ones and the disappearance of plasmonic hot spots. Consequently, the optical absorption is reduced when a long sputtering time is used [42].

We examined the crystallization of MAPbBr$_3$ from the DMF solution induced by irradiating Au nanoislands prepared with different sputtering times ($T = 20$, 30, and 40 s) by using 800-nm femtosecond laser pulses. The transmission spectra of the irradiation area measured at different laser powers are shown in Fig. 3(a-c) for the three samples, respectively. The bright-field images of the MAPbBr$_3$ observed at different laser powers are also presented. The threshold laser
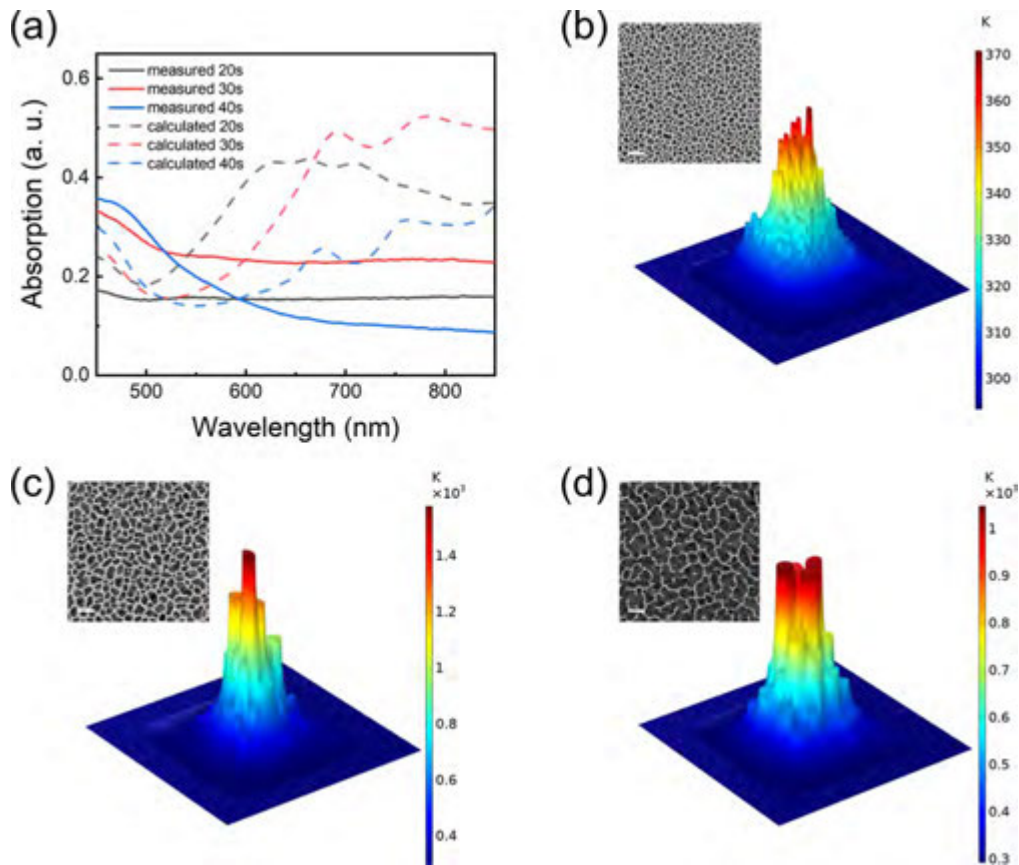
Fig. 2. (a) Measured and calculated absorption spectra for densely-packed Au nanoislands prepared by different sputtering times. The corresponding temperature distributions simulated for densely-packed Au nanoislands are shown in (b), (c) and (d), respectively. In all cases, the size of the simulation region is chosen to be 500×500 nm^2. The TEM images for Au nanoislands are shown in the insets. The length of the scale bar is 100 nm.

powers for creating a stable MAPbBr$_3$ crystal were found to be $P = 12$, 10, and 18 mW when Au nanoislands with $T = 20$, 30, 40 s were employed. This observation is anticipated from the larger optical absorption of the Au nanoislands with $T = 30$ s. It is noticed that a small dip appears at ~525 nm in the transmission spectra once the MAPbBr$_3$ is created. It is caused by the absorption of MAPbBr$_3$ crystal. For Au nanoislands with $T = 10$ and 50 s, no MAPbBr$_3$ crystal was formed even if the laser power was raised to $P = 30$ mW. Therefore, it is confirmed that the most efficient crystallization of MAPbBr$_3$ can be achieved by using Au nanoislands with $T = 30$ s. In Fig. 3(e), we present the dependences of the optical absorption of the Au film and the corresponding threshold laser power for the crystallization of MAPbBr$_3$ crystal on the sputtering time. It shows clearly that the largest optical absorption and the lowest threshold laser power are achieved in the sample with T = 30 s.

Since MAPbBr$_3$ crystal was induced by a laser beam in a microscope, it remains a big challenge to measure the X-ray diffraction spectrum of such a MAPbBr$_3$ crystal. As an alternative, we firstly used 325-nm laser light to induce a MAPbBr$_3$ crystal with a small size. Then, we employed 633-nm laser light to measure the Raman spectrum of the MAPbBr$_3$ crystal, as shown in Fig. 3(e) (purple curve). By comparing the Raman peaks appearing in the spectrum with those reported in
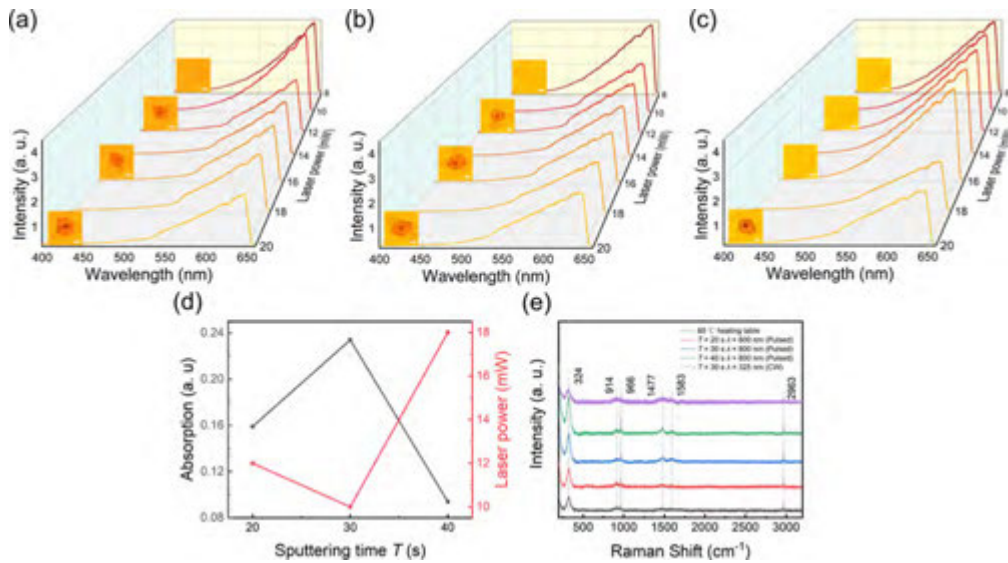
Fig. 3. Transmission spectra measured for Au nanoislands irradiated by laser beam at different powers. The Au nanoislands are prepared by different sputtering times of (a) $T = 20$ s, (b) $T = 30$ s and (c) $T = 40$ s. The bright-field images of the irradiation areas recorded by using a CCD are shown as insets. The length of the scale bar is $10 \, \mu m$. (d) Dependences of the optical absorption of the Au film and the threshold laser power for the crystallization of $MAPbBr_3$ crystal on the sputtering time. (e) Raman spectra measured for the $MAPbBr_3$ crystals fabricated under different conditions (colored curves). The Raman spectrum of the $MAPbBr_3$ crystal prepared by using a heating table is also provided for comparison (black curve).

the literature [48], it was confirmed that the synthesized material is a $MAPbBr_3$ crystal. We also measured the Raman spectra of the $MAPbBr_3$ crystals with larger sizes fabricated under different conditions (see black, red, blue, and green curves in Fig. 3(e)). Similarly, we observed all the Raman peaks reported for $MAPbBr_3$ crystal.

In Fig. 4(a), we show the transmission spectra of the irradiated area obtained at different laser powers for Au nanoislands with $T = 20$ s. One can see a reduction of the transmittance at $P = 12$ mW when the $MAPbBr_3$ crystal emerges from the solution. In particular, a small dip is found at ~525 nm, corresponding to the absorption peak of $MAPbBr_3$. In order to show more clearly the change of transmittance at ~525 nm, we normalized the transmission spectra in the presence of the laser light with respect to that in the absence of the laser light, as shown in Fig. 4(b). In this way, the formation of $MAPbBr_3$ is clearly reflected in the reduction of the transmittance at ~525 nm, which induces a transmission valley. When the laser power is further increased, the transmission valley becomes shallow due mainly to the decomposition of $MAPbBr_3$ at high laser powers [49,50]. In Fig. 4(c-j), we show the optical images of the irradiated area recorded at $P = 10$ mW. One can see the formation of a $MAPbBr_3$ crystal with a diameter of ~ $1.82 \, \mu m$ around the focal point (marked as a blue spot) at $t = 1.0$ s. The TPL from the $MAPbBr_3$ crystal, which appears as bright yellow light, is also observed. The diameter of the crystal is increased to ~$8.10 \, \mu m$ at $t = 2.0$ and 3.0 s. At $t = 4.0$ s, the size of the $MAPbBr_3$ crystal begins to decrease. It means that the heat generated by laser irradiation of Au nanoislands and the $MAPbBr_3$ crystal itself is not enough to maintain the stable existence of the $MAPbBr_3$ crystal. In this case, the $MAPbBr_3$ crystal is dissolved back into the solution. At $t = 5.0$ s, one can see the brightest TPL from the crystal. It is probably caused by the resonant excitation or emission from

the crystal. In this case, a strongly enhanced electric field at the excitation wavelength (800 nm) or the emission wavelength (~535 nm) is expected. For $t > 6.0$ s, the MAPbBr$_3$ crystal disappears completely, leaving some residues on the surface of Au nanoislands. For $P = 12$ mW, the formed MAPbBr$_3$ crystal can be stably maintained around the focal point with a diameter of ~ 11.57 μm, as shown in Fig. 4(k-r). In this case, the TPL from the MAPbBr$_3$ crystal is very weak. For $P < 3.0$ mW, no MAPbBr$_3$ crystal can be induced due to the low temperature at the focal point.
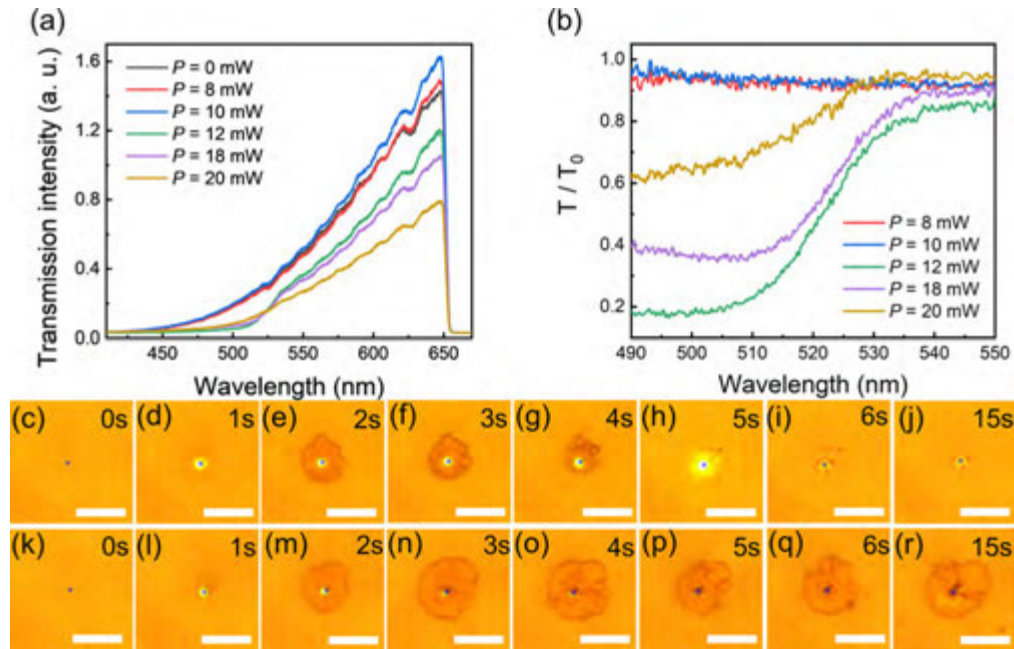

Fig. 4. (a) Transmission spectra measured for MAPbBr$_3$ crystals induced by laser light with different powers on Au nanoislands. (b) Normalized transmission spectra shown in (a) with respect to that in the absence of laser light. The bright-field images of MAPbBr$_3$ crystals induced by laser light with $P = 10$ mW (c – j) and $P = 12$ mW (k – r) on Au nanoislands at different irradiation times. The length of the scale bar is 10 μm.

To gain a deep insight into the growth process of the perovskite, we chose Au nanoislands with $T = 30$ s as the substrate for the DMF solution and varied the laser power from 0 to 20 mW. Upon the excitation of Au nanoislands with 800-nm femtosecond laser light, a MAPbBr$_3$ crystal is created around the focal point. Such a crystal can be stably maintained when the laser power exceeds $P = 10$ mW.

In order to reveal the dynamics for the crystallization of perovskite, we examined the evolution of the luminescence spectrum of the perovskite with increasing irradiation time. In Fig. 5(a), we present the luminescence spectra observed at different irradiation times when the laser power was chosen to be $P = 14$ mW. For $t = 0.5$ s, the luminescence of the MAPbBr$_3$ crystal appears at ~535 nm with a linewidth of ~26.76 nm. It is blueshifted to ~520 nm and broadened to ~45.71 nm at $t = 1.0$ s. The intensity remains nearly unchanged. However, a dramatic reduction in the luminescence intensity is observed at $t = 1.5$ s. Meanwhile, the luminescence peak is further shifted to ~515 nm. In this case, the perovskite is completely decomposed [49]. The crystallization and decomposition processes of the MAPbBr$_3$ crystal are accelerated at high laser powers, as shown in Fig. 5(b), where the luminescence spectra recorded at different times are presented for $P = 20$ mW. In this case, the luminescence peak at ~520 nm appears even at $t = 0.5$ s and its intensity is similar to that at ~535 nm. The coexistence of the two phases leads to the

two peaks in the luminescence spectrum. At $t = 1.0$ s, the luminescence peak at ~535 disappears and that at ~525 nm decreases. Only the luminescence peak at ~515 nm is left at $t = 1.5$ s.

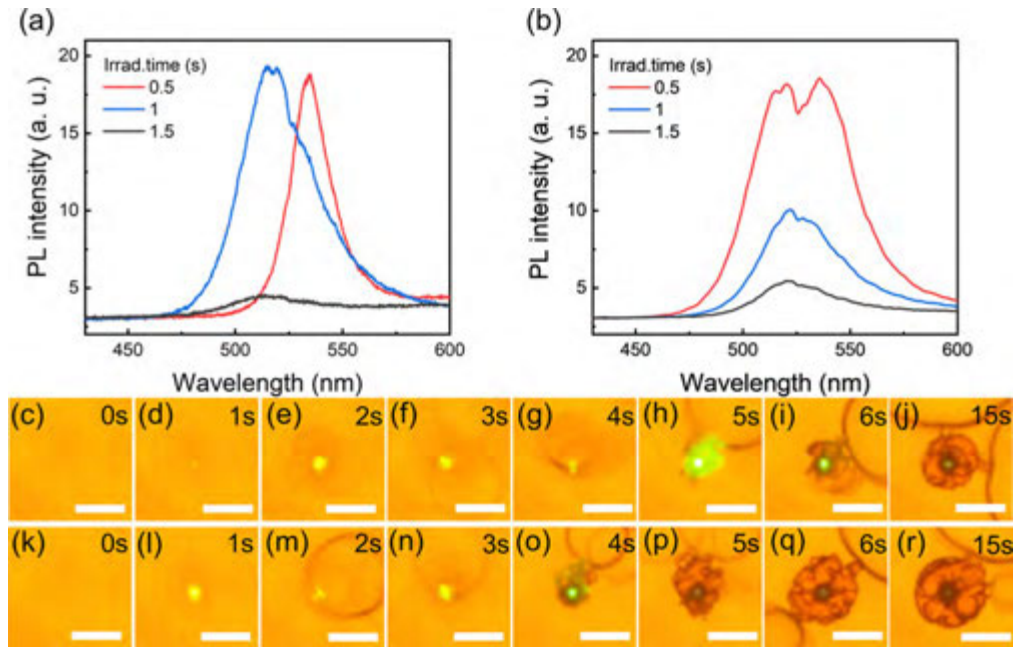**Fig. 5.** Evolutions of the PL spectra of the MAPbBr$_3$ crystals induced by laser light with $P = 14$ mW (a) and $P = 20$ mW (b). The bright-field images of MAPbBr$_3$ crystals induced by laser light with $P = 10$ mW (c – j) and $P = 12$ mW (k – r) on Au nanoislands at different irradiation times. The length of the scale bar is 10 μm.

Upon the irradiation of femtosecond laser light, crystallization of perovskite occurs at the focal point of the laser beam. As a result, one can see the TPL from the perovskite. However, the heat generated from nonradiative recombination of carriers leads to the rapid decomposition of the perovskite [49,50]. The residue left at the beam center results in the reduction in the transmittance, similar to that shown in Fig. 4(a). For Au nanoislands with $T = 30$ s, the perovskite can be stably maintained around the laser spot at $P = 10$ mW, as shown in Fig. 5(c-j). This behavior was not observed for Au nanoislands with $T = 20$ s. Thus, a lower threshold laser power required for introducing and maintaining a perovskite around the laser beam. With increasing laser power, the size of the perovskite created around the laser beam was also increased, as shown in Fig. 5(k-r) where the dynamical crystallization of perovskite induced by a laser beam with $P = 12$ mW is presented.

By using Au nanoislands with $T = 30$ s, the MAPbBr$_3$ crystal at the beam center will be completely decomposed under the continuous irradiation of the laser light. However, the MAPbBr$_3$ crystal around the laser spot can be stably maintained for a long time. This behavior offers us the opportunity for controllably and reversibly inducing the crystallization of perovskites by using laser irradiation. In Fig. 6(a), we show the luminescence spectra measured for the irradiated area at different time by using a laser beam with $P = 20$ mW. The corresponding optical images recorded by using a charge coupled device (CCD) are presented in Fig. 6(b-i). In this experiment, the laser light was switched off at $t = 30$ s. For $t = 10$ s, it can be seen that a MAPbBr$_3$ crystal with a diameter of ~14.96 μm was created around the laser spot at which the luminescence of the perovskite (green light) was clearly observed. This situation is stably maintained at $t = 30$ s. During this period, it is expected that the crystallization and dissolution of the perovskite

occur simultaneously at the periphery of the perovskite. These two processes lead eventually to an equilibrium state and the size of the perovskite remains almost unchanged. The time for establishing such an equilibrium is less than $t = 10$ s. The continuous irradiation will lead to the decomposition of the perovskite, as shown in Fig. 5(a). We turned off the laser light at $t = 30$ s, the MAPbBr$_3$ crystal was dissolved rapidly into the solution, as shown Fig. 6(f-i). During this period, one can see the gradual increase of the transmission at the long wavelengths, as shown in Fig. 6(a).
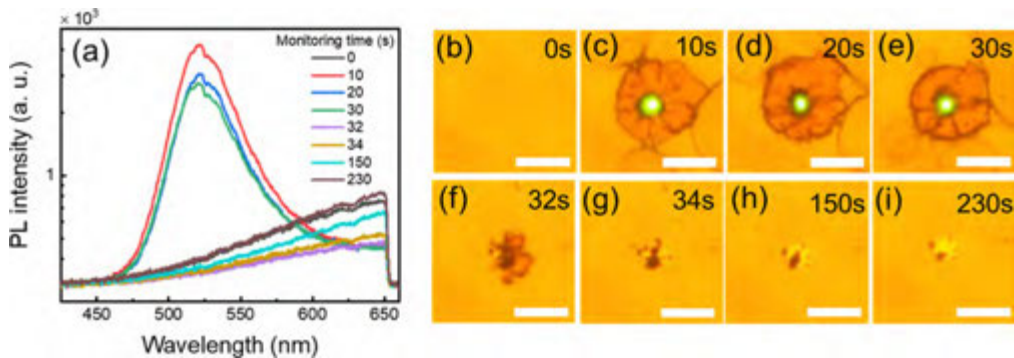

Fig. 6. (a) PL spectra measured for MAPbBr$_3$ crystals induced by laser light with $P = 20$ mW at different monitoring times. (b-i) Bright-field images of MAPbBr$_3$ crystals induced by laser light with $P = 20$ mW at different monitoring times. The length of the scale bar is 10 μm.

Actually, the concentration of the precursors plays a crucial role in determining the crystallization dynamics of the perovskite. In this work, we increased the concentration of the precursors from 1.0 to 1.8 M and examined the crystallization behavior by using laser powers ranging from 0 to 12 mW. It was found that the saturated concentration of the solution is ∼1.8 M. For solutions with concentrations smaller than 1.8 M, the crystallization behavior remained almost unchanged. However, the time for dissolving the crystal back into the solution was increased rapidly with increasing concentration. Interestingly, a different crystallization behavior was observed for the solution with a concentration of ∼1.8 M. The continuous growth of the crystal was observed upon the irradiation of the laser light, as shown in Fig. 7(a-e). Surprisingly, the perovskite was not dissolved back into the solution after switching off the laser light. Instead, a few microrods came out from the crystal and became longer and longer with time, as shown in Fig. 7(f-j).

We monitored the growth of a microrod, as shown in Fig. 8(a-c). It was found that the growth rate of the rod-like crystal along the long side is much faster than that along the short side. Within half an hour, a perovskite microrod with a width of a few microns and a length up to hundreds of microns was obtained. It was found that the morphologies of the perovskites prepared by using the ITC method were influenced by the concentration of the precursors [46]. It was reported previously that supersaturated solution induced by volatilization leads to the gradual precipitation of organic-inorganic hybrid perovskite nanowires in the solution [51–54]. For organic-inorganic hybrid halide perovskites, there is a strict stoichiometric ratio between the organic and inorganic components. The lattice structure of an organic-inorganic hybrid perovskite closely is related to the tolerance factor of the perovskite capacity [55]. Since the structure of the perovskite crystallized in solution is influenced by the sizes of the constituent ions, organic-inorganic hybrid perovskite nanowires can precipitate from a supersaturated solution. Here, the laser-induced perovskite acts as the seed for the further precipitation of the perovskite from the supersaturated solution. Consequently, a continuous growth of the perovskite into a microrod is achieved even after turning off the laser light.
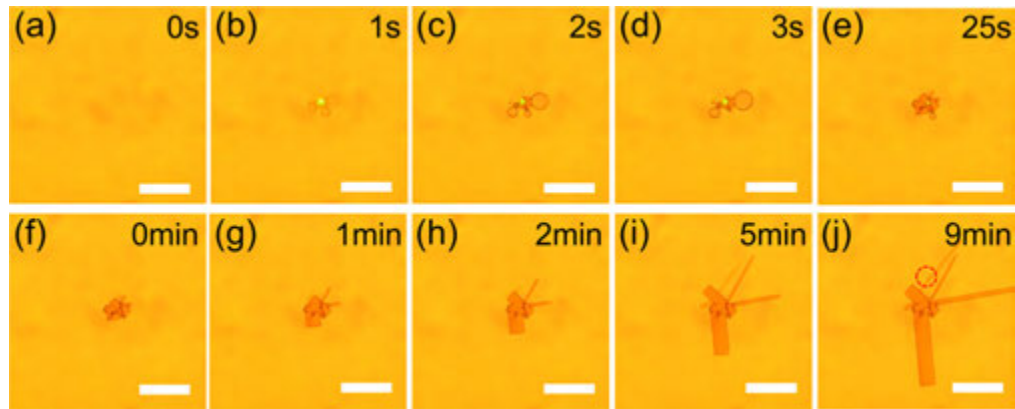
Fig. 7. (a-e) Bright-field images of MAPbBr$_3$ crystals induced by laser light with $P = 4$ mW Au nanoislands at different irradiation times. (f-j) Time-dependent bright-field images of MAPbBr$_3$ crystals after switching off the laser light. The length of the scale bar is 30 µm.
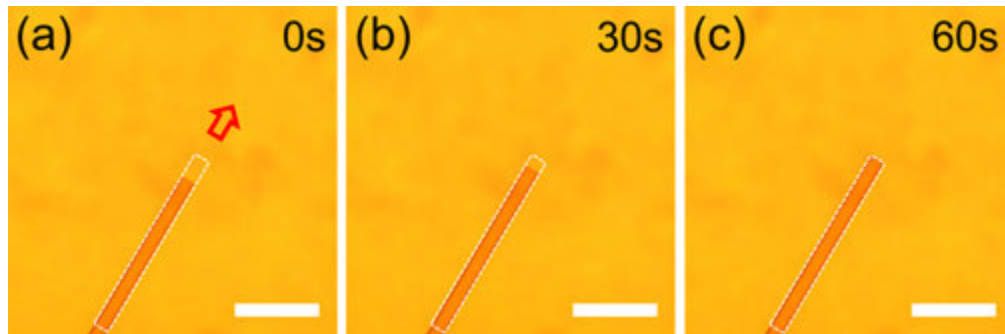

Fig. 8. (a-c) Time-dependent bright-field images of a MAPbBr$_3$ microrod after switching off the laser light. The length of the scale bar is 5.0 µm.

We examined the scattering and luminescence spectra of a MAPbBr$_3$ microrod prepared by using the method describe above, as shown in Fig. 9(a). The scattering spectrum is quite similar to that shown in Fig. 4(a). The scattering intensities at short wavelengths are greatly attenuated due to the absorption of the perovskite. The optical image of the perovskite microrod under a dark-field microscope is shown in the inset of Fig. 9(a). The luminescence peak of the perovskite was observed at ~535 nm under the excitation of 800-nm femtosecond laser light. It was found that the quality of the MAPbBr$_3$ microrods was improved by using laser-induced crystallization due to the reduction of polycrystalline. The image of the perovskite microrod excited by using femtosecond laser light is shown in the inset of Fig. 9(a). One can see the radiation from the end of the microrod when it was excited in the middle because the microrod serves as a waveguide for the luminescence [51]. No scattering light was observed during the propagation of the luminescence, indicating the MAPbBr$_3$ microrod possesses a smooth surface. In Fig. 9(b), we show the luminescence spectra measured for a MAPbBr$_3$ microrod at different laser powers. A slope of ~2.08 was derived if we plot the luminescence intensity as a function of laser power in a logarithmic coordinate, as shown in Fig. 9(c). The quadratic dependence of the luminescence intensity on laser power verifies the TPL nature of the luminescence from the MAPbBr$_3$ microrod excited by femtosecond laser light.
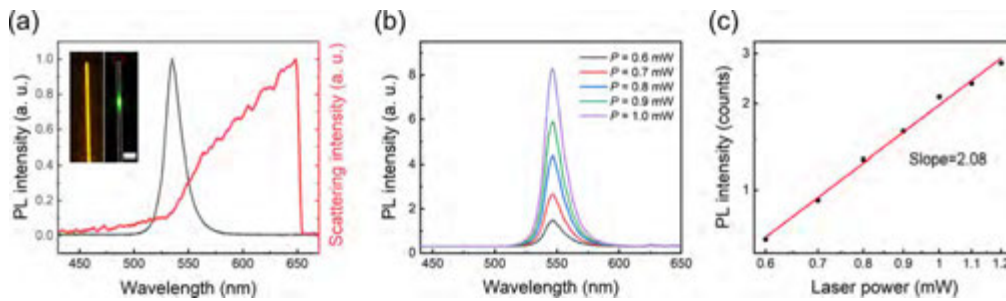
Fig. 9. (a) Scattering and PL spectra measured for a MAPbBr$_3$ microrod. Dark-field imgage (left) and luminescence image (right) of the MAPbBr$_3$ microrod recorded by using a CCD are shown as insets. The length of the scale bar is 2.0 μm. (b) PL spectra measured for the MAPbBr$_3$ microrod grown by laser irradiation. (c) Dependence of the luminescence intensity of the MAPbBr$_3$ microrod on the laser power plotted in a logarithmic coordinate.

In this work, we utilized the so-called ITC (inverse-temperature crystallization) method to induce the crystallization of MAPbBr$_3$. Physically, the synthesis of MAPbBr$_3$ crystal is caused by the local heating of Au nanoislands induced by laser irradiation. Therefore, it can be realized by not only femtosecond laser light but also continuous wave (CW) laser light. The only difference is the heating efficiency which determines the threshold laser power for the crystallization of MAPbBr$_3$. Physically, the heating efficiency is governed by the absorption of Au nanoislands. In fact, we have used CW laser light at 325 nm to do the same experiment. The threshold laser power was found to be ∼150 μW. Apart from MAPbBr$_3$ microrods, MAPbBr$_3$ thin films were also obtained by using solutions with higher concentrations. Based on scanning electron microscopy (SEM) observation, the thickness of such a MAPbBr$_3$ thin film was found to be a few micrometers.

4. Conclusions

In summary, we successfully demonstrated controllable and reversible crystallization of MAPbBr$_3$ by using laser irradiation assisted by densely-packed Au nanoislands. It was found that MAPbBr$_3$ crystals with finite sizes can be stably maintained at the focal point of the laser beam with a sufficiently large laser power. The threshold laser power for inducing the crystallization of MAPbBr$_3$ crystal depends on the morphology of Au nanoislands. High-quality MAPbBr$_3$ microrods can be obtained by simply increasing the concentration of the precursors in the laser-induced crystallization. Our findings open a new avenue for studying the crystallization dynamics of perovskites and pave the way for construct photonic functional devices based on perovskites.

Disclosures. All authors declare no conflict of interest.

Data availability. Data underlying the results presented in this paper are not publicly available at this time but may be obtained from the authors upon reasonable request.

References

1. J. J. Yoo, G. Seo, M. R. Chua, T. G. Park, Y. Lu, F. Rotermund, Y. K. Kim, C. S. Moon, N. J. Jeon, J. P. Correa-Baena, V. Bulovic, S. S. Shin, M. G. Bawendi, and J. Seo, "Efficient perovskite solar cells via improved carrier management," Nature **590**(7847), 587–593 (2021).
2. M. Kim, J. Jeong, H. Lu, T. K. Lee, F. T. Eickemeyer, Y. Liu, I. W. Choi, S. J. Choi, Y. Jo, H. B. Kim, S. I. Mo, Y. K. Kim, H. Lee, N. G. An, S. Cho, W. R. Tress, S. M. Zakeeruddin, A. Hagfeldt, J. Y. Kim, M. Gratzel, and D. S. Kim,

"Conformal quantum dot-SnO$_2$ layers as electron transporters for efficient perovskite solar cells," Science **375**(6578), 302–306 (2022).

3. P.-Y. Chen and S.-H. Yang, "Improved efficiency of perovskite solar cells based on Ni-doped ZnO nanorod arrays and Li salt-doped P3HT layer for charge collection," Opt. Mater. Express **6**(11), 3651–3669 (2016).

4. X. K. Liu, W. Xu, S. Bai, Y. Jin, J. Wang, R. H. Friend, and F. Gao, "Metal halide perovskites for light-emitting diodes," Nat. Mater. **20**(1), 10–21 (2021).

5. Z. Liu, W. Qiu, X. Peng, G. Sun, X. Liu, D. Liu, Z. Li, F. He, C. Shen, Q. Gu, F. Ma, H. L. Yip, L. Hou, Z. Qi, and S. J. Su, "Perovskite light-emitting diodes with EQE exceeding 28% through a synergetic dual-additive strategy for defect passivation and nanostructure regulation," Adv. Mater. (Weinheim, Ger.) **33**(43), 2103268 (2021).

6. W. Zhang, W. Yang, P. Zhong, S. Mei, G. Zhang, G. Chen, G. He, and R. Guo, "Spectral optimization of color temperature tunable white LEDs based on perovskite quantum dots for ultrahigh color rendition," Opt. Mater. Express **7**(9), 3065–3076 (2017).

7. Q. Zhang, Q. Shang, R. Su, T. T. H. Do, and Q. Xiong, "Halide perovskite semiconductor lasers: materials, cavity design, and low threshold," Nano Lett. **21**(5), 1903–1914 (2021).

8. F. Zhao, A. Ren, P. Li, Y. Li, J. Wu, and Z. M. Wang, "Toward continuous-wave pumped metal halide perovskite lasers: strategies and challenges," ACS Nano **16**(5), 7116–7143 (2022).

9. C. Qin, A. S. D. Sandanayaka, C. Zhao, T. Matsushima, D. Zhang, T. Fujihara, and C. Adachi, "Stable room-temperature continuous-wave lasing in quasi-2D perovskite films," Nature **585**(7823), 53–57 (2020).

10. B. Huang, J. Yi, G. Jiang, L. Miao, W. Hu, C. Zhao, and S. Wen, "Passively Q-switched vectorial fiber laser modulated by hybrid organic−inorganic perovskites," Opt. Mater. Express **7**(4), 1220–1227 (2017).

11. G. Dai, L. Wang, S. Cheng, Y. Chen, X. Liu, L. Deng, and H. Zhong, "Perovskite quantum dots based optical Fabry-Pérot pressure sensor," ACS Photonics **7**(9), 2390–2394 (2020).

12. H. Wang and D. H. Kim, "Perovskite-based photodetectors: materials and devices," Chem. Soc. Rev. **46**(17), 5204–5236 (2017).

13. Z. Rao, W. Liang, H. Huang, J. Ge, W. Wang, and S. Pan, "High sensitivity and rapid response ultraviolet photodetector of a tetragonal CsPbCl3 perovskite single crystal," Opt. Mater. Express **10**(6), 1374–1382 (2020).

14. S.-T. Ha, C. Shen, J. Zhang, and Q. Xiong, "Laser cooling of organic-inorganic lead halide perovskites," Nature Photonics **10**(2), 115–121 (2016).

15. B. J. Roman, N. M. Villegas, K. Lytle, and M. Sheldon, "Optically cooling cesium lead tribromide nanocrystals," Nano Lett. **20**(12), 8874–8879 (2020).

16. W. Zhang, Y. Ye, C. Liu, J. Wang, J. Ruan, X. Zhao, and J. Han, "Two-step anti-stokes photoluminescence of CsPbX$_3$ nanocrystals," Adv. Optical Mater. **9**(6), 2001885 (2021).

17. G. Xing, N. Mathews, S. Sun, S. S. Lim, Y. M. Lam, M. Gratzel, S. Mhaisalkar, and T. C. Sum, "Long-range balanced electron- and hole-transport lengths in organic-inorganic CH$_3$NH$_3$PbI$_3$," Science **342**(6156), 344–347 (2013).

18. J. H. Noh, S. H. Im, J. H. Heo, T. N. Mandal, and S. I. Seok, "Chemical management for colorful, efficient, and stable inorganic-organic hybrid nanostructured solar cells," Nano Lett. **13**(4), 1764–1769 (2013).

19. M. R. Filip, G. E. Eperon, H. J. Snaith, and F. Giustino, "Steric engineering of metal-halide perovskites with tunable optical band gaps," Nat. Commun. **5**(1), 5757 (2014).

20. V. D'Innocenzo, A. R. Srimath Kandada, M. De Bastiani, M. Gandini, and A. Petrozza, "Tuning the light emission properties by band gap engineering in hybrid lead halide perovskite," J. Am. Chem. Soc. **136**(51), 17730–17733 (2014).

21. D. Shi, V. Adinolfi, R. Comin, M. Yuan, E. Alarousu, A. Buin, Y. Chen, S. Hoogland, A. Rothenberger, K. Katsiev, Y. Losovyj, X. Zhang, P. A. Dowben, O. F. Mohammed, E. H. Sargent, and O. M. Bakr, "Solar cells. Low trap-state density and long carrier diffusion in organolead trihalide perovskite single crystals," Science **347**(6221), 519–522 (2015).

22. Z. Yang, Y. Deng, X. Zhang, S. Wang, H. Chen, S. Yang, J. Khurgin, N. X. Fang, X. Zhang, and R. Ma, "High-Performance Single-Crystalline Perovskite Thin-Film Photodetector," Adv. Mater. **30**(8), 1704333 (2018).

23. H. Jing, R. Peng, R. M. Ma, J. He, Y. Zhou, Z. Yang, C. Y. Li, Y. Liu, X. Guo, Y. Zhu, D. Wang, J. Su, C. Sun, W. Bao, and M. Wang, "Flexible Ultrathin Single-Crystalline Perovskite Photodetector," Nano Lett. **20**(10), 7144–7151 (2020).

24. J. He, C. Y. Li, D. X. Qi, Q. Cai, Y. Liu, R. H. Fan, J. Su, P. Huo, T. Xu, R. Peng, and M. Wang, "Improving Photoelectric Conversion with Broadband Perovskite Metasurface," Nano Lett. **22**(16), 6655–6663 (2022).

25. D. Wang, W. B. Shi, H. Jing, C. Yin, Y. Zhu, J. Su, G. B. Ma, R. Peng, X. Wang, and M. Wang, "Photon-induced carrier recombination in the nonlayered-structured hybrid organic-inorganic perovskite nano-sheets," Opt. Express **26**(21), 27504–27514 (2018).

26. M. I. Saidaminov, A. L. Abdelhady, B. Murali, E. Alarousu, V. M. Burlakov, W. Peng, I. Dursun, L. F. Wang, Y. He, G. Maculan, A. Goriely, T. Wu, O. F. Mohammed, and O. M. Bakr, "High-quality bulk hybrid perovskite single crystals within minutes by inverse temperature crystallization," Nat. Commun. **6**(1), 7586 (2015).

27. S. Wang and T. Ding, "Photothermal-assisted optical stretching of gold nanoparticles," ACS Nano **13**(1), 32–37 (2019).

28. Y. X. Wang, F. Ren, and T. Ding, "Generation of high quality, uniform and stable plasmonic colorants via laser direct writing," Adv. Optical Mater. **8**(12), 2000164 (2020).

29. R. Kamarudheen, G. Kumari, and A. Baldi, "Plasmon-driven synthesis of individual metal@semiconductor core@shell nanoparticles," Nat. Commun. **11**(1), 3957 (2020).

30. H. Li, X.-F. Li, C.-Y. Zhang, S.-L. Tie, and S. Lan, "Narrow titanium oxide nanowires induced by femtosecond laser pulses on a titanium surface," Applied Surface Science **396**, 221–225 (2017).

31. P. Wen, Y. Xu, S. Li, Z. Sun, M. Panmai, J. Xiang, S. Tie, and S. Lan, "Two-dimensional closely-packed gold nanoislands: A platform for optical data storage and carbon dot generation," Applied Surface Science **555**, 149586 (2021).

32. Y. Zheng, H. Liu, J. Li, J. Xiang, M. Panmai, Q. Dai, Y. Xu, S. Tie, and S. Lan, "Controllable formation of luminescent carbon quantum dots mediated by the Fano resonances formed in oligomers of gold nanoparticles," Adv. Mater. **31**(30), 1901371 (2019).

33. E. Cortes, L. V. Besteiro, A. Alabastri, A. Baldi, G. Tagliabue, A. Demetriadou, and P. Narang, "Challenges in plasmonic catalysis," ACS Nano **14**(12), 16202–16219 (2020).

34. S. C. Wang, H. L. Liu, J. Hu, L. Jiang, W. Liu, S. J. Wang, S. Zhang, J. G. Yin, and J. G. Lu, "In situ synthesis of NiO@Ni micro/nanostructures as supercapacitor electrodes based on femtosecond laser adjusted electrochemical anodization," Appl. Surf. Sci. **541**, 148216 (2021).

35. E. Oksenberg, I. Shlesinger, A. Xomalis, A. Baldi, J. J. Baumberg, A. F. Koenderink, and E. C. Garnett, "Energy-resolved plasmonic chemistry in individual nanoreactors," Nat. Nanotechnol. **16**(12), 1378–1385 (2021).

36. S. Wang, J. Yao, J. Ou, X. Wang, Y. Long, J. Zhang, Z. Fang, T. Wang, T. Ding, and H. Xu, "Plasmon-assisted nanophase engineering of titanium dioxide for improved performances in single-particle based sensing and photocatalysis," Nanoscale **14**(12), 4705–4711 (2022).

37. F. Chen, Y. Wang, S. Wang, B. Zhai, X. Lu, B. Sun, and T. Ding, "Plasmon-Assisted Nanopoling of Poly(Vinyl Difluoride) Films," Adv. Optical Mater. **9**(10), 2100084 (2021).

38. X. Wang, C. Zhang, F. Chen, J. Xiang, S. Wang, Z. Liu, and T. Ding, "Optically Triggered Nanoscale Plasmonic Dynamite," ACS Nano **16**(9), 13667–13673 (2022).

39. H. Tuxun, Z. Cai, M. Ji, B. Zhang, C. Zhang, J. Li, X. Yu, Z. Fu, Z. Zhang, and H. Zheng, "Controlling and probing heat generation in an optical heater system," Nanophotonics **11**(5), 979–986 (2022).

40. T. Kong, C. Zhang, J. Lu, B. Kang, Z. Fu, J. Li, L. Yan, Z. Zhang, H. Zheng, and H. Xu, "An enhanced plasmonic photothermal effect for crystal transformation by a heat-trapping structure," Nanoscale **13**(8), 4585–4591 (2021).

41. M. L. Brongersma, N. J. Halas, and P. Nordlander, "Plasmon-induced hot carrier science and technology," Nat. Nanotechnol. **10**(1), 25–34 (2015).

42. W. J. Zhuang, S. L. Li, F. Deng, G. C. Li, S. L. Tie, and S. Lan, "Laser writing of CsPbBr3 nanocrystals mediated by closely-packed Au nanoislands," Appl. Surf. Sci. **538**, 148143 (2021).

43. X. Huang, Q. Guo, D. Yang, X. Xiao, X. Liu, Z. Xia, F. Fan, J. Qiu, and G. Dong, "Reversible 3D laser printing of perovskite quantum dots inside a transparent medium," Nat. Photonics **14**(2), 82–88 (2020).

44. K. Leng, I. Abdelwahab, I. Verzhbitskiy, M. Telychko, L. Chu, W. Fu, X. Chi, N. Guo, Z. Chen, Z. Chen, C. Zhang, Q. H. Xu, J. Lu, M. Chhowalla, G. Eda, and K. P. Loh, "Molecularly thin two-dimensional hybrid perovskites with tunable optoelectronic properties due to reversible surface relaxation," Nat. Mater. **17**(10), 908–914 (2018).

45. G. Maculan, A. D. Sheikh, A. L. Abdelhady, M. I. Saidaminov, M. A. Haque, B. Murali, E. Alarousu, O. F. Mohammed, T. Wu, and O. M. Bakr, "CH3NH3PbCl3 single crystals: inverse temperature crystallization and visible-blind UV-photodetector," J. Phys. Chem. Lett. **6**(19), 3781–3786 (2015).

46. J. Zhang, K. Wang, Q. Yao, Y. Yuan, J. Ding, W. Zhang, H. Sun, C. Shang, C. Li, T. Zhou, and S. Pang, "Carrier diffusion and recombination anisotropy in the MAPbI3 single crystal," ACS Appl. Mater. Interfaces **13**(25), 29827–29834 (2021).

47. I. Pastoriza-Santos and L. M. Liz-Marzan, "N,N-dimethylformamide as a reaction medium for metal nanoparticle synthesis," Adv. Funct. Mater. **19**(5), 679–688 (2009).

48. J. Xing, X. Zheng, Z. Yu, Y. Lei, L. Hou, Y. Zou, C. Zhao, B. Wang, H. Yu, D. Pan, Y. Zhai, J. Cheng, D. Zhou, S. Qu, J. Yang, R. A. Ganeev, W. Yu, and C. Guo, "Dramatically Enhanced Photoluminescence from Femtosecond Laser Induced Micro-/Nanostructures on MAPbBr3 Single Crystal Surface," Advanced Optical Materials **6**(20), 1800411 (2018).

49. C. X. Zhang, T. Shen, D. Guo, L. M. Tang, K. Yang, and H. X. Deng, "Reviewing and understanding the stability mechanism of halide perovskite solar cells," InfoMat **2**(6), 1034–1056 (2020).

50. S. H. Turren-Cruz, A. Hagfeldt, and M. Saliba, "Methylammonium-free, high-performance, and stable perovskite solar cells on a planar architecture," Science **362**(6413), 449–453 (2018).

51. J. Wang, X. Jia, Y. Guan, K. Ren, H. Yu, Z. Wang, S. Qu, Q. Yang, J. Lin, Z. Wang, and P. Jin, "The electron-hole plasma contributes to both plasmonic and photonic lasing from CH3NH3PbBr3 nanowires at room temperature," Laser Photonics Rev **15**(6), 2000512 (2021).

52. E. Horvath, M. Spina, Z. Szekrenyes, K. Kamaras, R. Gaal, D. Gachet, and L. Forro, "Nanowires of methylammonium lead iodide (CH3NH3PbI3) prepared by low temperature solution-mediated crystallization," Nano Lett. **14**(12), 6761–6766 (2014).

53. L. Gao, K. Zeng, J. Guo, C. Ge, J. Du, Y. Zhao, C. Chen, H. Deng, Y. He, H. Song, G. Niu, and J. Tang, "Passivated single-crystalline CH3NH3PbI3 nanowire photodetector with high detectivity and polarization sensitivity," Nano Lett. **16**(12), 7446–7454 (2016).

54. P. Zhu, S. Gu, X. Shen, N. Xu, Y. Tan, S. Zhuang, Y. Deng, Z. Lu, Z. Wang, and J. Zhu, "Direct conversion of perovskite thin films into nanowires with kinetic control for flexible optoelectronic devices," Nano Lett. **16**(2), 871–876 (2016).

55. Y. Y. Dang, D. X. Ju, L. Wang, and X. T. Tao, "Recent progress in the synthesis of hybrid halide perovskite single crystals," Crystengcomm. **18**(24), 4476–4484 (2016).